

Learning Hydro-Phoretic Interactions in Active Matter

Palash Bera,¹ Aritra K. Mukhopadhyay,¹ and Benno Liebchen^{1,*}

¹*Institute for Condensed Matter Physics, Technische Universität Darmstadt, Hochschulstraße 8, 64289 Darmstadt, Germany.*

(Dated: January 6, 2026)

In the quest to understand large-scale collective behavior in active matter, the complexity of hydrodynamic and phoretic interactions remains a fundamental challenge. To date, most works either focus on minimal models that do not (fully) account for these interactions, or explore relatively small systems. The present work develops a generic method that combines high-fidelity simulations with symmetry-preserving descriptors and neural networks to predict hydro-phoretic interactions directly from particle coordinates (effective interactions). This method enables, for the first time, self-contained particle-only simulations and theories with full hydro-phoretic pair interactions.

Introduction.— One of the central fascinations of synthetic active matter is its ability to show intriguing self-organized behaviors in systems that are simpler, more controllable, and better reproducible than their biological counterparts. Prime examples include dynamic and chiral clustering at low density [1–15], activity-induced structure formation in active-passive mixtures [16–21], and the formation of active molecules that acquire motility from nonreciprocally interacting building blocks [22–29].

While significant progress has been made in identifying possible and highly plausible explanations for the mechanisms underlying these and many other phenomena, the state-of-the-art of our understanding of large scale behavior in active matter still largely hinges on phenomenological minimal models. These models often do not account for the full interactions among active particles to explain experimentally observed phenomena from first principles. In particular, many of the above-quoted phenomena, from dynamic clustering [2, 3, 5, 30] to rotating gears [10–13], and active molecules [25–27] are now known to strongly depend on hydrodynamic and phoretic interactions [31–41], which play a key role across active matter setups, from active colloids [31–41] to active droplets [42–47], and ion-exchange driven microswimmers [23, 48–50]. Thus, to understand collective behavior beyond minimal models, one would need to fully resolve hydro-phoretic interactions among all particles. In practice, fully resolved approaches, in which both hydrodynamic and phoretic fields are computed in the entire fluid domain and the relevant particle-field boundary conditions are accurately resolved at the surfaces of all particles, are currently feasible only for $\lesssim 10$ particles [51–57] and $\lesssim 10^2$ particles in dilute suspensions [58]. For sufficiently regular geometries, moderate system sizes of $\sim 10^2$ particles [59, 60] (and $\sim 10^4–10^5$ particles in diffusion-dominated regimes [61, 62]) can be reached based on reduced surface-based descriptions, such as boundary-integral or Galerkin methods, which approximately reconstruct hydrodynamic and phoretic interactions from analytically known Green’s functions or surface modes. Alternatively, systems with $\sim 10^3–10^4$ par-

ticles have been explored based on Lattice-Boltzmann-models [63, 64] that approximate particle field boundary conditions on a (static) grid, or, by representing hydro-phoretic fields by effective particles and using multi-particle collision dynamics [65, 66]. In all these approaches, scalability comes at the expense of significant discretization effects and/or a limited near-field resolution of hydro-phoretic interactions. Analytical theories describing large-scale collective behavior of active matter, in turn, currently account for hydro-phoretic far-field interactions at most; see e.g. [31, 32, 67–70].

To enable fully realistic analytical theories and very large simulations of phoretic active matter, we are currently lacking a method to eliminate hydro-phoretic fields from detailed models and to replace their net effect with effective interactions depending on particle coordinates only. This situation is in contrast to equilibrium, where effective interactions have been successfully determined for many different problems, based on the systematic reduction of partition functions of multicomponent systems to single species models [71], which are at the heart of much of what we know about equilibrium soft matter physics. In addition, very recently, innovative learning approaches have been developed as an alternative way to determine effective interactions. However, these methods have so-far been used for equilibrium problems and active matter models with prescribed short-range interactions only [72–86]. This leaves us with a fundamental knowledge gap regarding effective hydro-phoretic interactions.

In this letter, we develop a general method to determine effective hydro-phoretic interactions in active systems, enabling self-contained particle-only models. This framework comprises three parts: (i) high-fidelity simulations resolving near- and far-field hydrodynamic and phoretic couplings, (ii) a machine learning based method to systematically learn an effective, coarse-grained representation of these interactions using invariant descriptors (Fig. 1a), and (iii) a coarse-grained Brownian dynamics (BD) simulation model, where hydro-phoretic interactions are encoded as effective forces and torques (Fig. 1b). This approach massively reduces

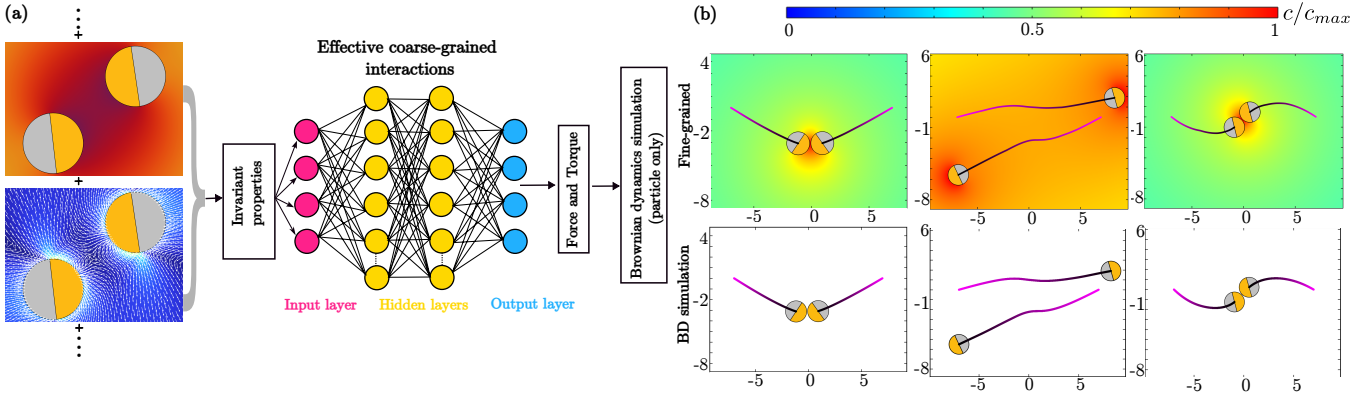


Figure 1. (a) Schematic of the coarse-graining method that extracts symmetry-preserving descriptors from fine-grained simulations (left) and feeds them into a deep artificial neural network (DNN). The DNN is trained to predict effective hydrodynamic and phoretic interactions directly from particle coordinates and enables self-contained Brownian dynamics simulations. (b) Comparison of fine-grained (top) and BD (bottom) trajectories. Background colors show the normalized phoretic field, and trajectory colors indicate time-evolution in arbitrary units. Left and middle panels: $\mu = 1$; right panel: $\mu = 0$.

the complexity of models with hydro-phoretic interactions. It enables a new kind of theories and simulations, treating field-mediated hydro-phoretic couplings as direct interparticle-interactions.

Main idea.— In this work, we focus on active colloids with instantaneous hydro-phoretic interactions, i.e., low Reynolds number (Stokes regime) and low solute Péclet number [31, 35, 87], as detailed below. In this regime, the timescale separation between the particle dynamics and the dynamics of the hydro-phoretic fields is complete, such that the instantaneous positions and orientations of all particles fully determine the phoretic and hydrodynamic fields. These fields, in turn, fully determine the velocities and angular velocities of all particles (up to thermal fluctuations and possible additional body forces, e.g., steric interactions). Thus, in principle, a mapping exists from particle positions and orientations to velocities and angular velocities (or effective forces and torques), enabling self-contained particle-only models. Establishing a method to explicitly determine such a mapping is the main goal of the present work. For simplicity, we focus on two-body interactions in bulk, but note that our approach is generic and can be generalized in the future to account for other factors that can influence hydro-phoretic interactions, such as the presence of substrates, bulk reactions, many-body effects, multiple phoretic fields, and irregular geometries [88–92].

Model.— We now describe our simulation model, that fully resolves the phoretic and hydrodynamic interactions in two self-diffusiophoretic Janus particles of radius R in two dimensions (2D) [31, 51, 88] (Fig. 2). Each particle, located at position \mathbf{r}_i with orientation θ_i ($i = \{1, 2\}$), features a catalytic hemisphere producing solute at a constant rate $\mathcal{A}(\mathbf{r}_{S_i}, t) = A$ and zero elsewhere, where \mathbf{r}_{S_i} denotes points on the particle surface S_i . The resulting solute concentration field $c(\mathbf{r}, t)$ obeys the

advection-diffusion equation $\partial_t c + \mathbf{u} \cdot \nabla c = D_c \nabla^2 c$, where D_c is the solute diffusion coefficient and $\mathbf{u}(\mathbf{r}, t)$ the local fluid velocity. We consider the low solute Péclet regime ($Pe_c = R|\mathbf{u}|/D_c \ll 1$), where solute diffusion dominates advection and the phoretic concentration field reaches a quasi-steady state satisfying $D_c \nabla^2 c = 0$, subject to the flux boundary condition $D_c \hat{\mathbf{n}} \cdot \nabla c|_{\mathbf{r}_{S_i}} = -\mathcal{A}(\mathbf{r}_{S_i}, t)$ and the far-field condition $c \rightarrow 0$ as $|\mathbf{r}| \rightarrow \infty$. Gradients in c generate phoretic slip flows at the particle surfaces, coupling the chemical and hydrodynamic fields. The fluid motion is described by the incompressible Stokes equations $\eta \nabla^2 \mathbf{u} = \nabla p$ and $\nabla \cdot \mathbf{u} = 0$, where η , \mathbf{u} , and p denote viscosity, velocity, and pressure, respectively. The slip boundary condition $\mathbf{u}_{\text{slip}}(\mathbf{r}_{S_i}) = \mathcal{M}(\mathbf{r}_{S_i}) \nabla_{||} c(\mathbf{r}_{S_i}, t)$ is applied on the surface of both the particles. This couples the phoretic and hydrodynamic fields, with surface mobility $\mathcal{M}(\mathbf{r}_{S_i}) = M_1$ at the catalytic hemisphere and M_2 at the neutral hemisphere. In our simulations, we consider both types of particles: with uniform mobility $M_1 = M_2$ and nonuniform mobility: $M_1 \neq M_2$. The tangential gradient is denoted by $\nabla_{||} = (\mathbf{I} - \hat{\mathbf{n}}\hat{\mathbf{n}}) \cdot \nabla$, where $\hat{\mathbf{n}}$ is the surface normal unit vector. The total surface velocity is $\mathbf{u}(\mathbf{r}_{S_i}, t) = \mathbf{v}_i + \boldsymbol{\Omega}_i \times \mathbf{r}_{S_i} + \mathbf{u}_{\text{slip}}(\mathbf{r}_{S_i})$, where \mathbf{v}_i and $\boldsymbol{\Omega}_i$ are the translational and rotational velocities of each particle. Far from the particle, the fluid is quiescent ($\mathbf{u} \rightarrow 0$ as $|\mathbf{r}| \rightarrow \infty$). Because self-propelled particles are force- and torque-free, \mathbf{v}_i and $\boldsymbol{\Omega}_i$ are determined by solving the coupled hydro-phoretic problem under the constraints of zero net hydrodynamic force and torque, ensuring momentum conservation [51, 88] (Fig. 2a). In the present case, the resulting interactions between the colloids are long-ranged and attractive.

We choose units of length, mass, time, and concentration as $l_u = R$, $m_u = \eta R^2 D_c / (AM_1)$, $t_u = RD_c / (AM_1)$, and $c_u = AR / D_c$, respectively [31]. This reduces the parameter space to two dimensions, spanned by the nondi-

dimensional mobility ratio $\mu = M_2/M_1$, and the solute Péclet number $Pe_c = AM_1R/D_c^2$, which we set to 0, to focus on the regime where phoretic interactions are instantaneous. We use finite element simulations with an adaptive moving mesh and an implicit backwards differentiation time-stepping formula (see SI for details). To show that our approach does not require a large training dataset, we simulate only $\sim 10^3$ distinct two-particle configurations starting from different relative orientations at fixed separations. We record the instantaneous positions and velocities of the Janus particles at each time step across far- and “near-field regimes” (interparticle distances $\lesssim R$, but still at distances where slip layers do not overlap).

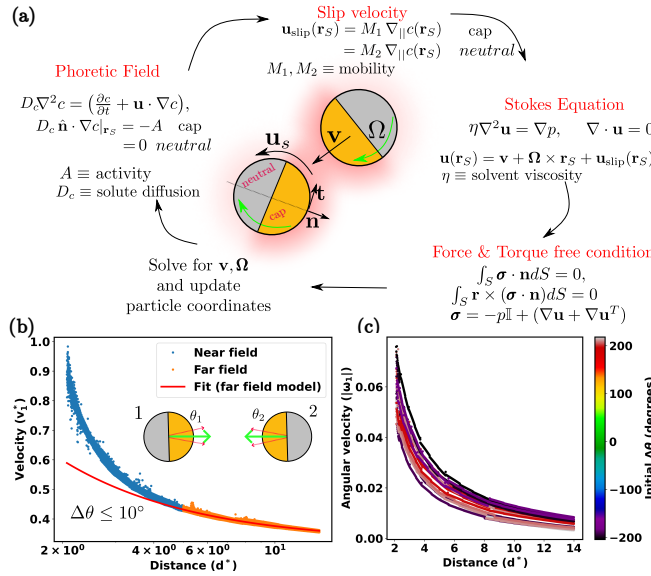


Figure 2. (a) Schematic of the fine-grained model that we solve numerically to determine the full hydrodynamic and phoretic interactions. (b) The velocity of colloid, v_1 , is fitted to $v_1 = \frac{a}{b+d} + v_0$, with fitting parameters a , b , and v_0 (see SI for details). The far-field regime is defined for $d > 5R$. The parameter v_0 corresponds to the self-propulsion velocity of an isolated colloid and the parameter: $\mu = 1$. The fitted velocity profiles scale as $1/d$ in the far field (red lines), whereas the near-field data reveal strong (orientation-dependent) deviations from this scaling, exemplarily shown for initial conditions, with particle orientations depicted in the inset. (c) Angular velocity as a function of interparticle distance for trajectories with parameter $\mu = 0$. The trajectories are color-coded according to their initial angle difference.

Fine-grained simulations.— Depending on the relative initial orientation of the particles $\Delta\theta = \theta_2 - \theta_1$ (Figs: 1b), we observe different types of trajectories. When two particles approach each other, they experience an effective attraction (Fig. 2b) either leading to binding or to scattering (Figs. 1b). In the case of nonuniform mobility, their angular velocities also increase (Fig. 2c). For large interparticle distances (far field), the relative veloc-

ity of the particles decays approximately as $\sim 1/d$ (Fig. 2b), where $d = |\mathbf{r}_2 - \mathbf{r}_1|$, characteristic of phoretic interactions [53, 55, 93]. For closer distances, the relative velocity increasingly depends on the relative particle orientation (Fig. 2b).

Learning approach.— Following the previously outlined idea of this work, we now determine particle velocities and angular velocities directly from positions and orientations, without solving hydrodynamic and phoretic equations. To achieve this, we use a fully connected feed-forward artificial deep neural network (DNN) (Fig. 1a). To construct a complete set of symmetry-invariant input features (feature vector), which we extract from the fine-grained simulations and feed into the input layer of the DNN, we first define the separation unit vector $\hat{\mathbf{r}} = (\mathbf{r}_2 - \mathbf{r}_1)/d$, its orthogonal complement $\hat{\mathbf{r}}_{\perp}$, and orientations vector $\mathbf{p}_{1,2} = (\cos \theta_{1,2}, \sin \theta_{1,2})$. The input features consist of d , the relative angular components $\cos(\Delta\theta)$ and $\sin(\Delta\theta)$ (where $\Delta\theta = \theta_2 - \theta_1$), and the projections of the particle orientations onto the interparticle axis: $\hat{\mathbf{r}} \cdot \mathbf{p}_{1,2}$ and $\hat{\mathbf{r}}_{\perp} \cdot \mathbf{p}_{1,2}$. The angular terms encode the alignment (parallel vs. antiparallel) and the chiral offsets, respectively. These descriptors ensure invariance under global transformations while preserving all required information. Accordingly, the DNN predicts the angular velocities and the translational velocity components projected onto the relative displacement vector: $v_{i\parallel} = \mathbf{v}_i \cdot \hat{\mathbf{r}}$ and $v_{i\perp} = \mathbf{v}_i \cdot \hat{\mathbf{r}}_{\perp}$. This projection guarantees that the target outputs are frame-invariant. Crucially, to enable the construction of many-body dynamics via pairwise summation, we isolate the interaction effects by training on the ‘excess’ velocity $\mathbf{v}_i - v_0 \mathbf{p}_i$, where v_0 is the self-propulsion speed determined from fully resolved single-particle simulations.

We use two independent, connected DNNs with identical architectures. The first network $f_{\Theta}^{(V)} : \mathbf{x} \mapsto \mathbf{V}$ maps the feature vector $\mathbf{x} \in \mathbf{R}^5$ to the velocities $\mathbf{V} = (v_{1\parallel}, v_{1\perp}, v_{2\parallel}, v_{2\perp}) \in \mathbf{R}^4$, while the second network $f_{\Theta}^{(\Omega)} : \mathbf{x} \mapsto \Omega$ predicts the angular velocities $\Omega = (\Omega_1, \Omega_2) \in \mathbf{R}^2$. Each network consists of three hidden layers with $H_1 = 32, H_2 = 64, H_3 = 32$ nodes, and exponential linear unit (elu) activations [94]. DNN parameters Θ (weights and biases) are optimized separately by minimizing the mean squared error loss function, $\mathcal{L} = \frac{1}{N_{\text{batch}}} \sum_{\text{batch}} \|\mathbf{y}^{\text{pred}} - \mathbf{y}^{\text{actual}}\|^2$, where $\mathbf{y}^{\text{pred}} = f_{\Theta}(\mathbf{x})$ denotes the network output and $\mathbf{y}^{\text{actual}}$ represents the ground-truth obtained from fine-grained simulations. Optimization is carried out using the Adam optimizer [95] with learning rate $\eta = 10^{-3}$. Training is performed for 500 epochs, and performance is evaluated on an independent test dataset to assess the network’s ability to generalize to unseen data (Figs: S1 a-f).

Coarse-grained model.— To assess the accuracy of the presented coarse-graining method, we now numerically solve the following equations of motion (Active

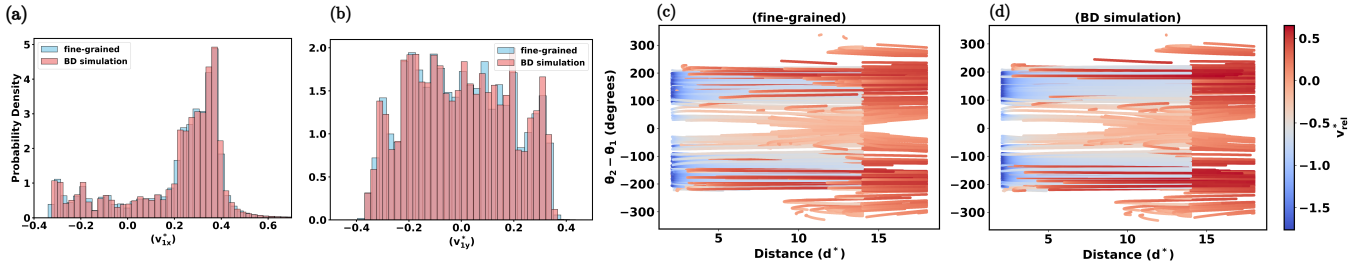


Figure 3. (a-b) Comparison of velocity distributions between fine-grained and coarse-grained BD simulations. (c-d) Relative velocity v_{rel}^* (in color) as a function of inter-particle distance d and relative orientation $\Delta\theta = \theta_2 - \theta_1$ for both fine-grained and coarse-grained BD simulations. Parameter for fine-grained model: $\mu = 1$. Parameters for coarse-grained model: $N = 2, v_0 = 0.345, \gamma = 1, D_t = D_r = 0.0, \epsilon = 0.0$.

Brownian particle model), starting with the same initial configuration as in the fine-grained simulations.

$$\dot{\mathbf{r}}_i = v_0 \mathbf{p}(\theta_i) + \sum_{\substack{j=1 \\ j \neq i}}^N \mathbf{v}_{i,j}^{nn} + \frac{1}{\gamma} \mathbf{F}_i^{\text{WCA}} + \sqrt{2D_t} \xi_i \quad (1)$$

$$\dot{\theta}_i = \sum_{\substack{j=1 \\ j \neq i}}^N \Omega_{i,j}^{nn} + \sqrt{2D_r} \zeta_i \quad (2)$$

Here $\mathbf{v}_{i,j}^{nn} \equiv v^{nn}(|\mathbf{r}_i - \mathbf{r}_j|, \theta_i, \theta_j)$ and $\Omega_{i,j}^{nn} \equiv \Omega^{nn}(|\mathbf{r}_i - \mathbf{r}_j|, \theta_i, \theta_j)$ denote the linear and angular velocities predicted by the neural networks, respectively, γ is the friction coefficient, and N is the total number of particles. $\mathbf{F}_i^{\text{WCA}}$ represents the Weeks-Chandler-Anderson (WCA) force [96], characterized by a repulsive force with strength $\epsilon = 10$ and a cutoff distance = 2.07, which is derived from the minimum inter-particle distance allowed in the two-particle fine-grained simulations. D_t and D_r are the translational and rotational diffusion coefficients, respectively, while ξ_i and ζ_i denote Gaussian white noise with zero mean and unit variance.

We first compare the distribution of velocity components between the fine-grained and coarse-grained models, which are in close quantitative agreement (Figs: 3a,b and Figs: S2 a,b). To additionally challenge the validity of our coarse-grained results, we now analyze the relative velocity $v_{rel}^* = (\mathbf{v}_2 - \mathbf{v}_1) \cdot \hat{\mathbf{r}}/v_0$ (color) for each individual trajectory, plotted as a function of inter-particle distance d and relative orientation $\Delta\theta$ in both fine-grained and coarse-grained BD simulations (Figs: 3c,d, and Figs: S3 a-d). Also here, the coarse-grained model closely agrees with the fine-grained data.

Many particle Brownian dynamics simulations.— To demonstrate how our method can be used to explore the collective behavior of active colloids, within a few hours on a desktop computer, we now perform many-particle BD simulations ($D_t = 0.01, D_r = 3D_t/4, \epsilon = 10, \mu \in \{0, 1\}$). We perform these simulations with random initial particle positions and orientations in a 2D box of size $L_x^* = 200, L_y^* = 200$ and periodic boundary conditions.

Perhaps unsurprisingly, for uniform mobility, $\mu = 1$, we observe that the particles form dense clusters (Figs: 4a,b and Video S1), even at a low packing fraction of $\phi = \frac{N\pi R^2}{4L_x L_y} = 0.1$. These clusters hardly rotate and slowly merge and grow (coarsen) over time. In contrast, for nonuniform mobility, $\mu = 0$, we observe substantial cluster rotations (Figs: 4c,d, S4, and Video S2), which occasionally make them dynamically break and reform. This is in close analogy to the celebrated but still partly mysterious experiments showing living/dynamic clustering [1-3]. This observation suggests that cluster rotations, induced by nonuniform surface mobility, could be key to finally understand the mechanism underlying dynamic clustering. Over long times, the individual cluster synchronize and all rotate clockwise or anticlockwise varying from simulation to simulation as will be studied separately.

Conclusions.— The presented method, to learn effective interactions from fine-grained simulations, enables self-contained particle-only models of active particles with fully representative hydrodynamic and phoretic interactions. These models could enable a new type of continuum theories and unprecedentedly large simulations of phoretic active matter. Notably, our method is highly generalizable and could help initiating a new era of formulating reduced models for complex nonequilibrium problems with complete timescale separation – also beyond active matter. Generalizations in the near future could account for substrate-mediated osmotic interactions, many-body effects, several phoretic fields, and bulk reactions. Finally, to explicitly enforce momentum conservation in the reduced particle-only model, one could add constraints such as force-balance corrections or feedback mechanisms.

This project was funded by the Deutsche Forschungsgemeinschaft (DFG, German Research Foundation) in the framework of the collaborative research center Multiscale Simulation Methods for Soft-Matter Systems (TRR 146) under Project No. 233630050.

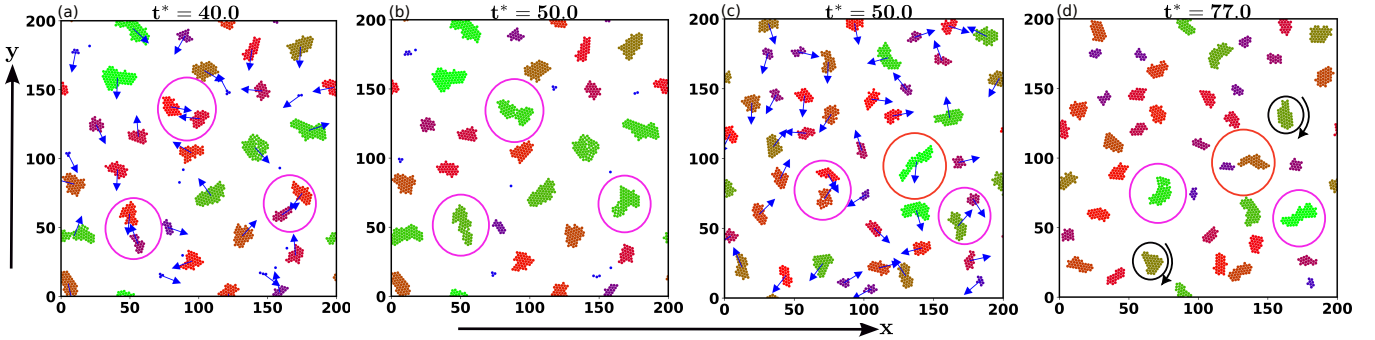


Figure 4. Snapshots from many-particle BD simulations with effective hydro-phoretic pair-interactions at packing fraction $\phi = 0.1$ for uniform ($\mu = 1$) (a-b) and nonuniform ($\mu = 0$) (c-d) surface mobility. Clusters are colored according to their size. Arrows indicate cluster translations and rotations. Over time, neighboring clusters merge (magenta circles), and for nonuniform surface mobility, they feature pronounced rotations (black circle), inducing their breakage and re-formation (orange circle). Parameters: $D_t = 0.01$, $D_r = 3D_t/4$, $\epsilon = 10$. The values of D_t and D_r are chosen such that $v_0/(RD_r) \sim 10^1 - 10^2$, as typical for autophasoretic Janus colloids in water.

* benno.liebchen@pkm.tu-darmstadt.de

- [1] F. Ginot, I. Theurkauff, F. Detcheverry, C. Ybert, and C. Cottin-Bizonne, “Aggregation-fragmentation and individual dynamics of active clusters,” *Nat Commun* **9**, 696 (2018).
- [2] J. Palacci, S. Sacanna, A. P. Steinberg, D. J. Pine, and P. M. Chaikin, “Living Crystals of Light-Activated Colloidal Surfers,” *Science* **339**, 936 (2013).
- [3] I. Theurkauff, C. Cottin-Bizonne, J. Palacci, C. Ybert, and L. Bocquet, “Dynamic Clustering in Active Colloidal Suspensions with Chemical Signaling,” *Phys. Rev. Lett.* **108**, 268303 (2012).
- [4] O. Pohl and H. Stark, “Dynamic Clustering and Chemo-tactic Collapse of Self-Phoretic Active Particles,” *Phys. Rev. Lett.* **112**, 238303 (2014).
- [5] I. Buttinoni, J. Bialké, F. Kümmel, H. Löwen, C. Bechinger, and T. Speck, “Dynamical Clustering and Phase Separation in Suspensions of Self-Propelled Colloidal Particles,” *Phys. Rev. Lett.* **110**, 238301 (2013).
- [6] Z. Peng and R. Kapral, “Self-organization of active colloids mediated by chemical interactions,” *Soft Matter* **20**, 1100 (2024).
- [7] S. Ketzetzi, L. Caprini, V. Willems, L. Alvarez, H. Löwen, and L. Isa, “Active Colloidal Molecules with Dynamic Configurational Freedom,” *ACS Nano* **19**, 29430 (2025).
- [8] L. Caprini, D. Breoni, A. Ldov, C. Scholz, and H. Löwen, “Dynamical clustering and wetting phenomena in inertial active matter,” *Commun Phys* **7**, 343 (2024).
- [9] P. Baconnier, O. Dauchot, V. Démery, G. Düring, S. Henkes, C. Huepe, and A. Shee, “Self-aligning polar active matter,” *Rev. Mod. Phys.* **97**, 015007 (2025).
- [10] A. Aubret, M. Youssef, S. Sacanna, and J. Palacci, “Targeted assembly and synchronization of self-spinning microgears,” *Nature Phys* **14**, 1114 (2018).
- [11] A. Aubret and J. Palacci, “Diffusiophoretic design of self-spinning microgears from colloidal microswimmers,” *Soft Matter* **14**, 9577 (2018).
- [12] A. Aubret, Q. Martinet, and J. Palacci, “Metamachines of pluripotent colloids,” *Nat Commun* **12**, 6398 (2021).
- [13] Q. Martinet, A. Aubret, and J. Palacci, “Rotation Control, Interlocking, and Self-Positioning of Active Cogwheels,” *Adv. Intell. Syst.* **5**, 2200129 (2023).
- [14] B. Liebchen and D. Levis, “Chiral active matter,” *EPL* **139**, 67001 (2022).
- [15] G. Gompper, H. A. Stone, C. Kurzthaler, D. Saintillan, F. Peruani, D. A. Fedosov, T. Auth, C. Cottin-Bizonne, C. Ybert, E. Clément, *et al.*, “The 2025 motile active matter roadmap,” *J. Phys.: Condens. Matter* **37**, 143501 (2025).
- [16] J. P. Steimel, J. L. Aragones, H. Hu, N. Qureshi, and A. Alexander-Katz, “Emergent ultra-long-range interactions between active particles in hybrid active-inactive systems,” *Natl. Acad. Sci. U.S.A.* **113**, 4652 (2016).
- [17] J. Smrek and K. Kremer, “Small Activity Differences Drive Phase Separation in Active-Passive Polymer Mixtures,” *Phys. Rev. Lett.* **118**, 098002 (2017).
- [18] J. Stenhammar, R. Wittkowski, D. Marenduzzo, and M. E. Cates, “Activity-Induced Phase Separation and Self-Assembly in Mixtures of Active and Passive Particles,” *Phys. Rev. Lett.* **114**, 018301 (2015).
- [19] J. Mason, R. L. Jack, and M. Bruna, “Dynamical patterns and nonreciprocal effective interactions in an active-passive mixture through exact hydrodynamic analysis,” *Nat Commun* **16**, 6017 (2025).
- [20] D. Boniface, S. G. Leyva, I. Pagonabarraga, and P. Tierno, “Clustering induces switching between phoretic and osmotic propulsion in active colloidal rafts,” *Nat Commun* **15**, 5666 (2024).
- [21] S. Williams, R. Jeanneret, I. Tuval, and M. Polin, “Confinement-induced accumulation and de-mixing of microscopic active-passive mixtures,” *Nat Commun* **13**, 4776 (2022).
- [22] R. Soto and R. Golestanian, “Self-Assembly of Catalytically Active Colloidal Molecules: Tailoring Activity Through Surface Chemistry,” *Phys. Rev. Lett.* **112**, 068301 (2014).
- [23] R. Niu, A. Fischer, T. Palberg, and T. Speck, “Dynamics of binary active clusters driven by ion-exchange particles,” *ACS nano* **12**, 10932 (2018).
- [24] J. Agudo-Canalejo and R. Golestanian, “Active Phase Separation in Mixtures of Chemically Interacting Particles,” *Nat Commun* **12**, 6398 (2021).

cles,” *Phys. Rev. Lett.* **123**, 018101 (2019).

[25] F. Schmidt, B. Liebchen, H. Löwen, and G. Volpe, “Light-controlled assembly of active colloidal molecules,” *J. Chem. Phys.* **150**, 094905 (2019).

[26] Z. Wang, Z. Wang, J. Li, C. Tian, and Y. Wang, “Active colloidal molecules assembled via selective and directional bonds,” *Nat Commun* **11**, 2670 (2020).

[27] J. Grauer, F. Schmidt, J. Pineda, B. Midtvedt, H. Löwen, G. Volpe, and B. Liebchen, “Active droploids,” *Nat Commun* **12**, 6005 (2021).

[28] S. Fehlinger and B. Liebchen, “Collective behavior of active molecules: Dynamic clusters, holes, and active fractalytes,” *Phys. Rev. Res.* **5**, L032038 (2023).

[29] S. Hara, M. Okada, K. Kittaka, S. Tanami, Y. Iwasaki, H. Ishikawa, K. Yoshii, and Y. Sumino, “Nonreciprocal interactions induce persistent active clusters in binary colloids,” (2025), arXiv:2509.23164 [cond-mat].

[30] F. Ginot, I. Theurkauff, F. Detcheverry, C. Ybert, and C. Cottin-Bizonne, “Aggregation-fragmentation and individual dynamics of active clusters,” *Nat. Commun.* **9**, 696 (2018).

[31] B. Liebchen and A. K. Mukhopadhyay, “Interactions in active colloids,” *J. Phys.: Condens. Matter* **34**, 083002 (2021).

[32] B. Liebchen and H. Löwen, “Synthetic Chemotaxis and Collective Behavior in Active Matter,” *Acc. Chem. Res.* **51**, 2982 (2018).

[33] A. Zöttl and H. Stark, “Modeling Active Colloids: From Active Brownian Particles to Hydrodynamic and Chemical Fields,” *Annu. Rev. Condens. Matter Phys.* **14**, 109 (2023).

[34] R. Golestanian, “Phoretic active matter,” (2019), arXiv:1909.03747 [cond-mat.soft].

[35] J. L. Moran and J. D. Posner, “Phoretic Self-Propulsion,” *Annu. Rev. Fluid Mech.* **49**, 511 (2017).

[36] P. Illien, R. Golestanian, and A. Sen, “‘Fuelled’ motion: Phoretic motility and collective behaviour of active colloids,” *Chem. Soc. Rev.* **46**, 5508 (2017).

[37] M. C. Marchetti, J. F. Joanny, S. Ramaswamy, T. B. Liverpool, J. Prost, M. Rao, and R. A. Simha, “Hydrodynamics of soft active matter,” *Rev. Mod. Phys.* **85**, 1143 (2013).

[38] C. Bechinger, R. Di Leonardo, H. Löwen, C. Reichhardt, G. Volpe, and G. Volpe, “Active particles in complex and crowded environments,” *Rev. Mod. Phys.* **88**, 045006 (2016).

[39] W. Wang, “Open Questions of Chemically Powered Nano- and Micromotors,” *J. Am. Chem. Soc.* **145**, 27185 (2023).

[40] C. Carrasco, Q. Martinet, Z. Shen, J. LiA regularised singularity approach to phoretic problemsntuori, J. Palacci, and A. Aubret, “Characterization of Nonequilibrium Interactions of Catalytic Microswimmers Using Phoretically Responsive Nanotracers,” *ACS Nano* **19**, 11133 (2025).

[41] X. Wang, P.-C. Chen, K. Kroy, V. Holubec, and F. Cichos, “Spontaneous vortex formation by microswimmers with retarded attractions,” *Nat. Commun.* **14**, 56 (2023).

[42] C. C. Maass, C. Krüger, S. Herminghaus, and C. Bahr, “Swimming Droplets,” *Annu. Rev. Condens. Matter Phys.* **7**, 171 (2016).

[43] K. Feng, J. C. Ureña Marcos, A. K. Mukhopadhyay, R. Niu, Q. Zhao, J. Qu, and B. Liebchen, “Self-Solidifying Active Droplets Showing Memory-Induced Chirality,” *Adv. Sci.* **10**, 2300866 (2023).

[44] W. Chen, A. Izzet, R. Zakine, E. Clément, E. Vandendriessche, and J. Brujic, “Evolving Motility of Active Droplets Is Captured by a Self-Repelling Random Walk Model,” *Phys. Rev. Lett.* **134**, 018301 (2025).

[45] N. Ziethen, J. Kirschbaum, and D. Zwicker, “Nucleation of Chemically Active Droplets,” *Phys. Rev. Lett.* **130**, 248201 (2023).

[46] S. Michelin, “Self-Propulsion of Chemically Active Droplets,” *Annu. Rev. Fluid Mech.* **55**, 77 (2023).

[47] K. E. Kim, R. V. Balaj, and L. D. Zarzar, “Chemical Programming of Solubilizing, Nonequilibrium Active Droplets,” *Acc. Chem. Res.* **57**, 2372 (2024).

[48] R. Niu and T. Palberg, “Modular approach to microswimming,” *Soft Matter* **14**, 7554 (2018).

[49] B. Liebchen, R. Niu, T. Palberg, and H. Löwen, “Unraveling modular microswimmers: From self-assembly to ion-exchange-driven motors,” *Phys. Rev. E* **98**, 052610 (2018).

[50] N. Möller, B. Liebchen, and T. Palberg, “Shaping the gradients driving phoretic micro-swimmers: influence of swimming speed, budget of carbonic acid and environment,” *Eur. Phys. J. E* **44**, 41 (2021).

[51] A. Varma and S. Michelin, “Modeling chemo-hydrodynamic interactions of phoretic particles: A unified framework,” *Phys. Rev. Fluids* **4**, 124204 (2019).

[52] P. Sharan, A. Daddi-Moussa-Ider, J. Agudo-Canalejo, R. Golestanian, and J. Simmchen, “Pair Interaction between Two Catalytically Active Colloids,” *Small* **19**, 2300817 (2023).

[53] B. Nasouri and R. Golestanian, “Exact Phoretic Interaction of Two Chemically Active Particles,” *Phys. Rev. Lett.* **124**, 168003 (2020).

[54] B. Nasouri and R. Golestanian, “Exact axisymmetric interaction of phoretically active Janus particles,” *J. Fluid Mech.* **905**, A13 (2020).

[55] N. Sharifi-Mood, A. Mozaffari, and U. M. Córdova-Figueroa, “Pair interaction of catalytically active colloids: From assembly to escape,” *J. Fluid Mech.* **798**, 910 (2016).

[56] F. Rojas-Pérez, B. Delmotte, and S. Michelin, “Hydrochemical interactions of phoretic particles: A regularized multipole framework,” *J. Fluid Mech.* **919**, A22 (2021).

[57] T. D. Montenegro-Johnson, S. Michelin, and E. Lauga, “A regularised singularity approach to phoretic problems,” *Eur. Phys. J. E* **38**, 139 (2015).

[58] Z. Gou, C. Misbah, and A. Farutin, “A computational framework for simulating suspensions of phoretic particles,” *J. Fluid Mech.* **1016**, A25 (2025).

[59] B. Delmotte and F. B. Usabiaga, “A scalable method to model large suspensions of colloidal phoretic particles with arbitrary shapes,” *J. Comput. Phys.* **518**, 113321 (2024).

[60] R. Kohl, E. Corona, V. Cheruvu, and S. Veerapaneni, “Fast and accurate solvers for simulating Janus particle suspensions in Stokes flow,” *Adv. Comput. Math.* **49**, 45 (2023).

[61] R. Singh and R. Adhikari, “PyStokes: Phoresis and Stokesian hydrodynamics in Python,” *Journal of Open Source Software* **5**, 2318 (2020).

[62] R. Singh, R. Adhikari, and M. E. Cates, “Competing chemical and hydrodynamic interactions in autophasoretic colloidal suspensions,” *J. Chem. Phys.* **151**, 044901 (2019).

[63] A. Scagliarini and I. Pagonabarraga, “*Unravelling the role of phoretic and hydrodynamic interactions in active colloidal suspensions*,” *Soft Matter* **16**, 8893 (2020).

[64] Q. Yang, M. Jiang, F. Picano, and L. Zhu, “*Shaping active matter from crystalline solids to active turbulence*,” *Nat. Commun.* **15**, 2874 (2024).

[65] B. Robertson, M.-J. Huang, J.-X. Chen, and R. Kapral, “*Synthetic nanomotors: working together through chemistry*,” *Acc. Chem. Res.* **51**, 2355 (2018).

[66] M.-J. Huang, J. Schofield, and R. Kapral, “*Chemotactic and hydrodynamic effects on collective dynamics of self-diffusiophoretic janus motors*,” *New J. Phys.* **19**, 125003 (2017).

[67] S. Saha, R. Golestanian, and S. Ramaswamy, “*Clusters, asters, and collective oscillations in chemotactic colloids*,” *Phys. Rev. E* **89**, 062316 (2014).

[68] P. Illien, R. Golestanian, and A. Sen, “*‘fuelled’ motion: phoretic motility and collective behaviour of active colloids*,” *Chem. Soc. Rev.* **46**, 5508 (2017).

[69] B. Liebchen, D. Marenduzzo, and M. E. Cates, “*Phoretic interactions generically induce dynamic clusters and wave patterns in active colloids*,” *Phys. Rev. Lett.* **118**, 268001 (2017).

[70] H. Stark, “*Artificial Chemotaxis of Self-Phoretic Active Colloids: Collective Behavior*,” *Acc. Chem. Res.* **51**, 2681 (2018).

[71] C. N. Likos, “*Effective interactions in soft condensed matter physics*,” *Phys. Rep.* **348**, 267 (2001).

[72] M. Ruiz-Garcia, C. M. Barriuso G., L. C. Alexander, D. G. A. L. Aarts, L. M. Ghiringhelli, and C. Valeriani, “*Discovering dynamic laws from observations: The case of self-propelled, interacting colloids*,” *Phys. Rev. E* **109**, 064611 (2024).

[73] J. Hem, A. Poncet, P. Ronceray, D. Nishiguchi, and V. Demery, “*Learning general pair interactions between self-propelled particles*,” *Soft Matter* (2025), 10.1039/D5SM00655D.

[74] Z. Han, D. S. Kammer, and O. Fink, “*Learning physics-consistent particle interactions*,” *PNAS Nexus* **1**, pgac264 (2022).

[75] F. Cichos, K. Gustavsson, B. Mehlig, and G. Volpe, “*Machine learning for active matter*,” *Nat Mach Intell* **2**, 94 (2020).

[76] T. ter Rele, G. Campos-Villalobos, R. van Roij, and M. Dijkstra, “*Machine learning many-body potentials for charged colloids in primitive 1:1 electrolytes*,” *J. Chem. Phys.* **163**, 164106 (2025).

[77] C. R. Rees-Zimmerman, J. Martín-Roca, D. Evans, M. A. Miller, D. G. A. L. Aarts, and C. Valeriani, “*Numerical methods for unraveling inter-particle potentials in colloidal suspensions: A comparative study for two-dimensional suspensions*,” *J. Chem. Phys.* **162**, 074103 (2025).

[78] S. Ha and H. Jeong, “*Unraveling hidden interactions in complex systems with deep learning*,” *Sci Rep* **11**, 12804 (2021).

[79] Y. Ji, J. Liang, and Z. Xu, “*Machine-Learning Interatomic Potentials for Long-Range Systems*,” *Phys. Rev. Lett.* **135**, 178001 (2025).

[80] J. Behler, “*Four Generations of High-Dimensional Neural Network Potentials*,” *Chem. Rev.* **121**, 10037 (2021).

[81] J. Behler and M. Parrinello, “*Generalized Neural-Network Representation of High-Dimensional Potential-Energy Surfaces*,” *Phys. Rev. Lett.* **98**, 146401 (2007).

[82] B. E. Husic, N. E. Charron, D. Lemm, J. Wang, A. Pérez, M. Majewski, A. Krämer, Y. Chen, S. Olsson, G. de Fabritiis, F. Noé, and C. Clementi, “*Coarse graining molecular dynamics with graph neural networks*,” *J. Chem. Phys.* **153**, 194101 (2020).

[83] J. Wang, S. Olsson, C. Wehmeyer, A. Pérez, N. E. Charron, G. de Fabritiis, F. Noé, and C. Clementi, “*Machine Learning of Coarse-Grained Molecular Dynamics Force Fields*,” *ACS Cent. Sci.* **5**, 755 (2019).

[84] M. Han, J. Devany, M. Fruchart, M. L. Gardel, and V. Vitelli, “*Learning noisy tissue dynamics across time scales*,” (2025), arXiv:2510.19090 [cond-mat].

[85] P. Bayati and S. A. Mallory, “*Inferring Surface Slip in Active Colloids from Flow Fields Using Physics-Informed Neural Networks*,” (2025), arXiv:2511.22723 [cond-mat].

[86] C. R. Rees-Zimmerman, C. M. B. G., C. Valeriani, and D. G. A. L. Aarts, “*Effective interactions in active Brownian particles*,” *Soft Matter* (2025), 10.1039/D5SM00706B.

[87] R. Golestanian, T. B. Liverpool, and A. Ajdari, “*Designing phoretic micro- and nano-swimmers*,” *New J. Phys.* **9**, 126 (2007).

[88] S. Michelin and E. Lauga, “*Phoretic self-propulsion at finite Péclet numbers*,” *J. Fluid Mech.* **747**, 572 (2014).

[89] S. Das, A. Garg, A. I. Campbell, J. Howse, A. Sen, D. Velezol, R. Golestanian, and S. J. Ebbens, “*Boundaries can steer active Janus spheres*,” *Nat. Commun.* **6**, 8999 (2015).

[90] J. Simmchen, J. Katuri, W. E. Uspal, M. N. Popescu, M. Tasinkevych, and S. Sánchez, “*Topographical pathways guide chemical microswimmers*,” *Nat. Commun.* **7**, 10598 (2016).

[91] E. Kanso and S. Michelin, “*Phoretic and hydrodynamic interactions of weakly confined autophasoretic particles*,” *J. Chem. Phys.* **150**, 044902 (2019).

[92] Y. Ibrahim, R. Golestanian, and T. B. Liverpool, “*Multiple phoretic mechanisms in the self-propulsion of a Pt-insulator Janus swimmer*,” *J. Fluid Mech.* **828**, 318 (2017).

[93] B. Liebchen and H. Löwen, “*Which interactions dominate in active colloids?*” *J. Chem. Phys.* **150** (2019).

[94] D.-A. Clevert, T. Unterthiner, and S. Hochreiter, “*Fast and accurate deep network learning by exponential linear units (elus)*,” (2016), arXiv:1511.07289 [cs.LG].

[95] D. P. Kingma and J. Ba, “*Adam: A method for stochastic optimization*,” (2017), arXiv:1412.6980 [cs.LG].

[96] J. D. Weeks, D. Chandler, and H. C. Andersen, “*Role of Repulsive Forces in Determining the Equilibrium Structure of Simple Liquids*,” *J. Chem. Phys.* **54**, 5237 (1971).

Supplemental Material: Learning Hydro-Phoretic Interactions in Active Matter

Palash Bera,¹ Aritra K. Mukhopadhyay,¹ and Benno Liebchen¹

¹ Institute for Condensed Matter Physics, Technische Universität Darmstadt, Hochschulstraße 8, 64289 Darmstadt, Germany.

Details of fine-grained numerical solutions

We numerically solved the fully coupled dimensionless equations of motion presented in the main text using the finite element software COMSOL Multiphysics with the PARDISO linear solver and an implicit backward differentiation formula (BDF) time-stepping scheme. A moving-mesh formulation accounts for the particle motion and shape deformation, while adaptive remeshing maintains numerical accuracy by refining the mesh whenever its quality falls below a predefined threshold 0.1. A very fine triangular mesh is used, with extra resolution in the interparticle region and near the particle boundaries.

Distance-dependent velocity fit for the active colloids

We fit the translational velocity of each Janus colloid, v_i , as a function of the interparticle separation $d = |\mathbf{r}_2 - \mathbf{r}_1|$ to the form

$$v_i(d) = \frac{a}{b + d} + v_0, \quad (1)$$

with a , b and v_0 being the fit parameters. We fit the velocity only in the far-field regime, defined by $d > 5R$, where R is the particle radius. In this regime, the fitted velocity profiles exhibit the expected $1/d$ scaling, consistent with long-range phoretic interactions (Fig. 2b, main text). At shorter separations, pronounced deviations from this scaling occur due to orientation-dependent near-field interactions. The fit parameters are obtained as follows: $a = 0.563$, $b = 0.018$, and $v_0 = 0.319$. The value of v_0 matches closely with the self-propulsion speed of the colloids obtained from our fine-grained simulations of a single isolated colloid.

Validation of DNN Predictions

To quantify the predictive accuracy of the DNN, we compute the Pearson correlation coefficient $\rho = \frac{\text{cov}(X^{\text{true}}, X^{\text{DNN}})}{\sqrt{\text{var}(X^{\text{true}}) \text{var}(X^{\text{DNN}})}}$, where X denotes either the velocity components of one of the particles ($v_{1\parallel}, v_{1\perp}, v_{2\parallel}, v_{2\perp}$) or the angular velocities (Ω_1, Ω_2). A value of $\rho = 1$ corresponds to perfect agreement, while $\rho = 0$ indicates random predictions. Additionally, we evaluate the root mean squared error, given by $\text{RMSE} = \sqrt{\frac{1}{N} \sum_{i=1}^N (X_i^{\text{true}} - X_i^{\text{DNN}})^2}$, where N is the number of test samples, to quantify the deviation between the predicted and “true” values from fine grained simulations. A lower RMSE value signifies better accuracy in the model’s predictions. As shown in Figs. S1(a-f), ρ is consistently close to unity for both velocity components and angular velocities across all test sets, indicating that the DNN successfully captures the underlying two-body hydro-phoretic interaction laws. The RMSE is correspondingly low, confirming the model’s strong predictive performance and its ability to generalize well to unseen data.

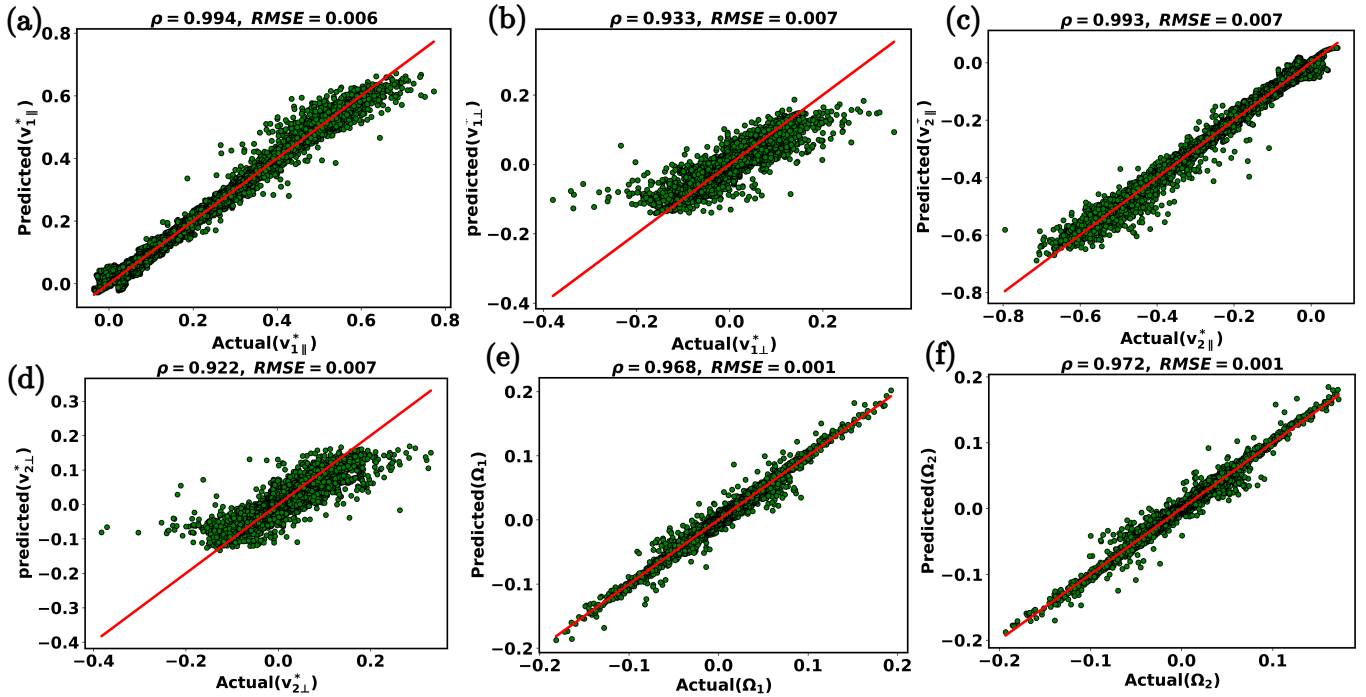


Figure S1. (a) Pearson correlation coefficient ρ for the DNN's predicted linear velocity (a-d) and angular velocity (e-f) components. The correlation between the true and predicted values for both linear and angular velocities is consistently close to unity across all test sets, indicating that the DNN effectively captures the underlying two-body hydro-phoretic interaction laws.

Comparison between fine-grained and BD simulations

We plot the probability distributions of the velocity components of the second particle obtained from fine-grained and coarse-grained Brownian dynamics simulations. Panels S2(a,b) show the corresponding distributions for the two Cartesian velocity components for 2nd particle. The coarse-grained results are in close quantitative agreement with the fine-grained data, demonstrating that the coarse-grained model accurately reproduces the single-particle velocities.

To gain better insights into the two-particle dynamics, we analyze the relative velocity $(\mathbf{v}_2 - \mathbf{v}_1) \cdot \hat{\mathbf{r}}$ for each individual trajectory, plotted as a function of inter-particle distance d and relative orientation $\Delta\phi = \phi_2 - \phi_1$ in both fine-grained and coarse-grained BD simulations. Depending on the sign of the relative velocity, we can separate the different modes of motion: particles approaching (negative relative velocity) and particles moving away (positive relative velocity) (Figs. S3(a-d)). The color maps show how these modes evolve with inter-particle distance and orientation. Notably, the coarse-grained simulations, which rely on the neural network model, show excellent agreement with the fully resolved fine-grained data.

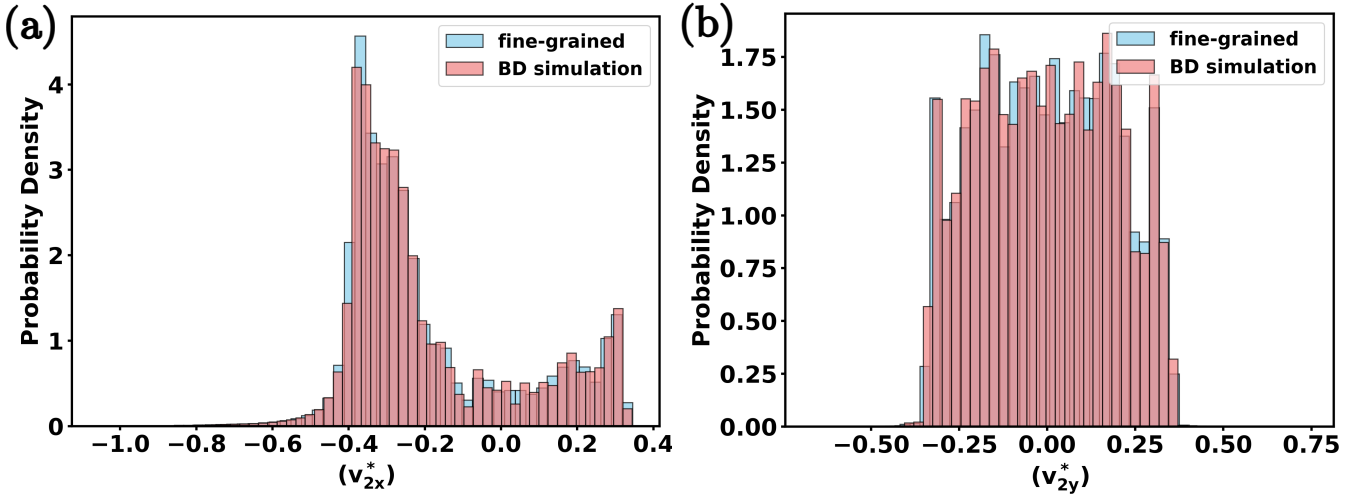


Figure S2. Comparison of velocity distributions between fine-grained and coarse-grained BD simulations for the 2nd particle. The velocity distributions for the active colloid in both simulations match closely, confirming that the DNN accurately captures the effective interactions without considering explicit field contributions.

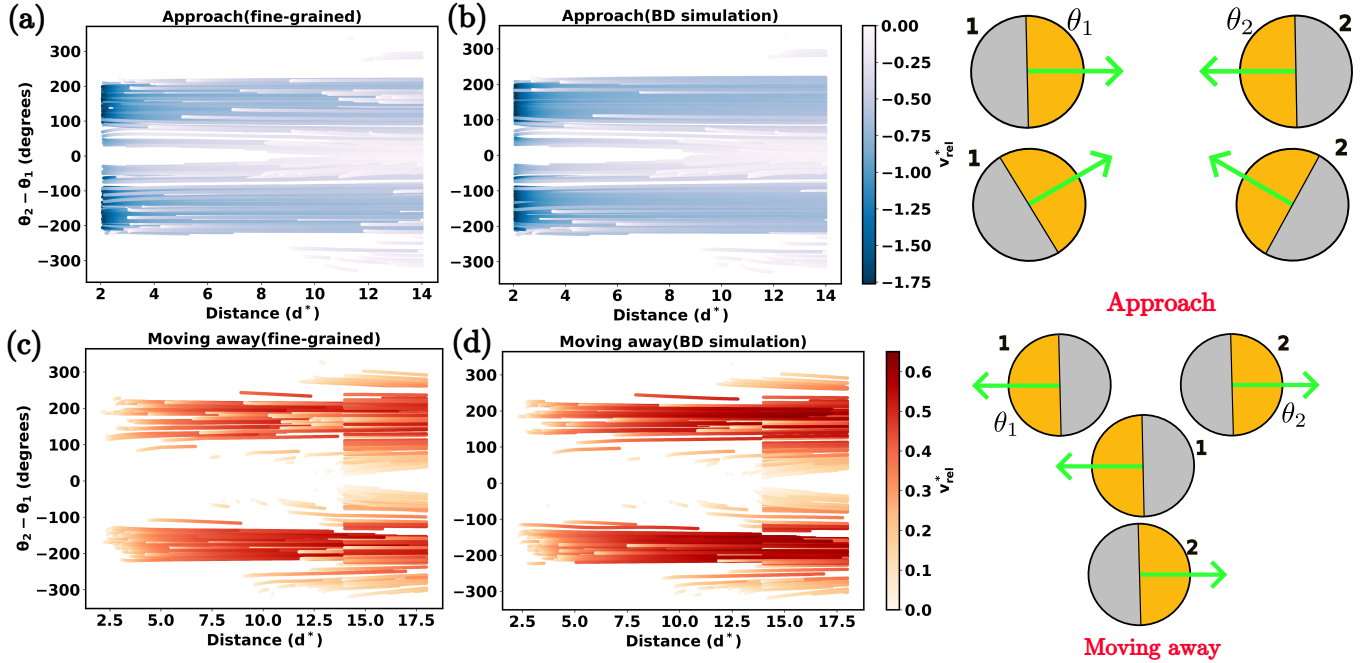


Figure S3. Relative velocity v_{rel} (in color) as a function of inter-particle distance d and relative orientation $\Delta\theta = \theta_2 - \theta_1$ for both fine-grained (a-b) and coarse-grained BD simulations (c-d). Depending on the sign of the relative velocity, we separate the different modes of motion, approaching (negative relative velocity) and moving away (positive relative velocity).

Spontaneous symmetry breaking

For nonuniform mobility, we observe the emergence of clockwise-rotating clusters, a phenomenon driven by spontaneous symmetry breaking. To confirm this, we analyzed time-lapse snapshots of the particles, tracking the evolution of the sign of their angular velocity (Ω) (Fig. S4). Initially, the system shows a disordered state with a balanced mixture of positive and negative Ω values. However, as the simulation progresses the particles aggregate, causing a transition where some individual clusters adopt a predominantly negative sign. This shift demonstrates how the

system breaks its initial rotational symmetry, leading to the formation of rotating clusters.

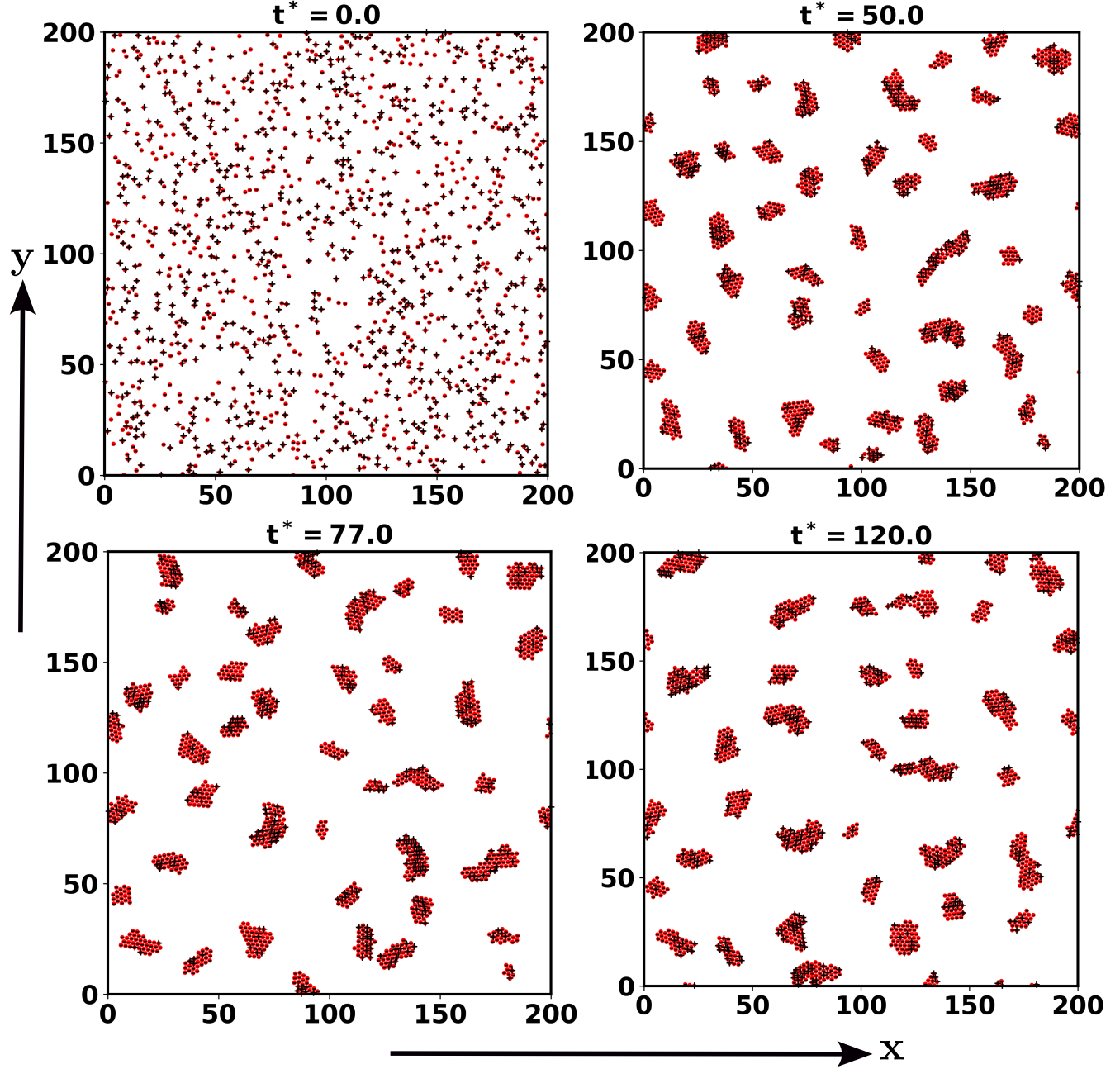


Figure S4. Emergence of rotating clusters due to spontaneous symmetry breaking for nonuniform mobility. Time-lapse snapshots show the evolution from a disordered state with mixed angular velocities to clustered states with a dominant (clockwise) rotation, evidencing spontaneous rotational symmetry breaking.

[List of movies](#)

1. **Many body simulations of particles with uniform surface mobility ($\mu = 1$).** Animated version of Fig. 4a,b (Video S1) showing the time evolution of many-particle Brownian dynamics simulations with effective hydro-phoretic interactions at packing fraction $\phi = 0.1$. The simulation parameters are $D_t = 0.01$, $D_r = 3D_t/4$, and $\epsilon = 10$.

2. **Many body simulations of particles with nonuniform surface mobility ($\mu = 0$).** Animated version of Fig. 4c,d (Video S2) showing the corresponding many-particle Brownian dynamics simulations at $\phi = 0.1$. In this case, clusters exhibit pronounced rotations, occasionally leading to their dynamic breakage and re-formation. The simulation parameters are $D_t = 0.01$, $D_r = 3D_t/4$, and $\epsilon = 10$.